Nitrogen-Doped Porous Carbon Cages for Electrocatalytic Reduction of Oxygen: Enhanced Performance with Iron and Cobalt Dual Metal Centers

Rene Mercado,[a] Carolin Wahl,[a] Jia En Lu,[a] Tianjun Zhang,[b] Bingzhang Lu,[a] Peng Zhang,[b] Jennifer Q. Lu,[c] A'Lester Allen,[a] Jin Z. Zhang,[a] and Shaowei Chen*[a]

Heteroatom-doped carbon materials are promising electrocatalysts towards the oxygen reduction reaction (ORR). In this study, dual metals (Fe an Co) and nitrogen-codoped porous carbon cages (CHS–FeCo) were synthesized by controlled pyrolysis of silica nanoparticle-supported melamine-formaldehyde resin embedded with iron and cobalt precursors, followed by acid etching. Transmission electron microscopy measurements confirmed the formation of hollow carbon cages, and the absence of metal (oxide) nanoparticles suggested atomic dispersion of the metal species within the mesoporous carbon skeletons. X-ray photoelectron spectroscopic analysis revealed a composition of mostly carbon, oxygen, and nitrogen, with ca. 1% metals. Electrochemically, the dual-metal ones showed a significant enhancement of the catalytic performance towards ORR in alkaline media, as compared to samples with single or no metal dopants. This was accounted for by the synergistic interaction between the Fe and Co centers in the carbon samples, as evidenced in X-ray absorption spectroscopic studies. Remarkably, the CHS–FeCo sample exhibited apparent resistance against KSCN poisoning, where XPS analysis revealed oxidation of KSCN and no metal-sulfur interaction, in sharp contrast to the Fe counterpart which was easily poisoned. Results from this study suggest that the synergistic interactions between dual metal centers may be exploited for enhanced ORR performance of carbon-based nanocomposite catalysts.

1. Introduction

In recent decades, proton exchange membrane fuel cells (PEMFCs) have gained a great deal of attention as potential power sources for diverse applications, not only due to their emission-free operation and utilization of non-fossil fuels, but also because hydrogen has a significantly higher energy density than regular gasoline and PEMFCs have a greater theoretical efficiency than combustion engines.[1] In order to achieve the efficiency, the electrochemical reactions taking place in the cell must do so with fast kinetics at low overpotentials. In PEMFCs, the oxygen reduction reaction (ORR) at the cathode has notoriously sluggish kinetics, and does hardly occur without effective catalysts, making this reaction a major obstacle for the large-scale commercialization of fuel cell technology.[2] Platinum-based catalysts have been shown to provide the necessary catalytic activity at sufficiently high mass loadings, but its low abundance and prohibitive cost limits their use in commercial settings.[3] A range of strategies have been examined to improve the ORR activity of Pt nanoparticles, which usually involve the manipulation of size, composition, and surface atomic arrangements of the catalysts.[4] In addition, extensive research efforts have also been devoted to the design and engineering of Pt-free catalysts. Of these, carbon-based materials have received increasing attention.[5] While pristine carbon materials are unable to achieve an activity comparable to that of commercial Pt, heteroatom dopants, such as nitrogen, are known to modulate the electronic properties and surface polarities of the carbon skeletons, and have been shown to greatly increase the ORR activity.[6] This is primarily because heteroatom doping induces a charge redistribution, thereby facilitating the adsorption of oxygen.[7]

With the embedment of select transition metal elements into the carbon skeletons, the ORR activity can be further enhanced.[8] Promising non-noble transition metals, such as iron, cobalt, nickel, and manganese, have been used in the design of carbon-based ORR catalysts, and are believed to make an essential contribution to the overall activity,[9] which is mostly ascribed to the formation of metal-nitrogen-carbon (MNC) coordinated structures, the so-called single atom catalysts.[9c,10] In these studies, the catalysts are generally prepared by controlled pyrolysis of metal and heteroatom-containing precursors,[11] and the ORR active sites are formed as the result of a series of heat treatment and etching steps.[9b,11a] It

[a] R. Mercado, C. Wahl, Dr. J. En Lu, B. Lu, A'L. Allen, Prof. J. Z. Zhang, Prof. S. Chen
Department of Chemistry and Biochemistry
University of California
1156 High Street
Santa Cruz, CA-95064 (USA)
E-mail: shaowei@ucsc.edu
[b] T. Zhang, Prof. P. Zhang
Department of Chemistry
Dalhousie University
6274 Coburg Road
Halifax, Nova Scotia B3H 4R2 (Canada)
[c] Prof. J. Q. Lu
School of Engineering
University of California
5200 North Lake Road
Merced, CA-95343 (USA)

Supporting information for this article is available on the WWW under https://doi.org/10.1002/cctc.201902324

is now broadly accepted that nitrogen-carbon structures that are active for ORR include various kinds of nitrogen defects in the carbon matrix, replacing sp^2-hybridized carbon atoms either at the edges (pyrrolic and pyridinic) or within the skeleton (graphitic); and the nitrogen dopants may serve as the coordinating environment for metal ions, forming the presumed active center MN_x for ORR.[12]

Interestingly, the ORR activity can be further enhanced by incorporating dual metal dopants into the carbon matrix (e.g., Fe, Co, Pt, Pd, and Ni),[13] where the synergistic interactions between the metal centers can be exploited to facilitate the adsorption and reduction of oxygen intermediates,[14] and it has recently been demonstrated that bimetallic systems, such as iron and cobalt, are among the most promising for the electroreduction of oxygen.[11d] In these carbon materials, FeN_x sites have been proposed as the active sites,[15] where the high spin state of iron is particularly attractive.[16] In addition to this, the enhanced corrosion resistance of cobalt[17] can have an influence on ORR in both acid and alkaline media. In one study,[18] Fe and Co were both incorporated in a mesoporous porphyrinic carbon structure (OMPCs), which exhibited an ORR activity that was markedly better than those of the monometal ones and comparable to Pt in acidic environments. This was ascribed to the bimetal interaction that had a synergistic effect on FeCo–OMPCs, which resulted in a weakened interaction with oxygen, as compared to the monometallic OMPCs and Pt.

The porosity of the catalyst materials is another important parameter that can impact the accessibility to the catalytic active centers and mass transfer of reaction species, and hence the ORR activity.[19] This can be manipulated by using select structural templates.[15a,20] In this study, we report the preparation of porous carbon cages codoped with nitrogen and dual metals of Fe and Co (CHS–FeCo), and observed a remarkable ORR activity in alkaline media, as compared to the metal-free samples or samples doped with a single metal species, which was accounted for by the synergistic interactions between the Fe and Co centers in the carbon matrix. In addition, the CHS–FeCo catalysts were found to exhibit apparent resistance against KSCN poisoning, in sharp contrast to the Fe counterpart that could be easily poisoned by KSCN.

2. Results and Discussion

In this study, the CHS–FeCo samples were prepared by using a three-step procedure (Figure 1): (i) SiO_2 nanoparticles were prepared and used as the rigid templates onto which a melamine-formaldehyde (MF) polymer layer is grown; (ii) the obtained SiO_2@MF nanoparticles were impregnated with select Fe and Co precursors, and underwent pyrolysis at controlled temperatures for carbonization of the polymer layers; and (iii) finally the SiO_2 templates were removed by chemical etching with HF, affording dual metals and nitrogen-codoped porous carbon cages (CHS–FeCo). In this procedure, melamine acted as the main carbon and nitrogen source, and formaldehyde used to crosslink the melamine monomers to each other and to the silica surface.[21] Three samples were prepared at different $FeSO_4$ and $CoCl_2$ loadings, CHS–FeCo(1), CHS–FeCo(2) and CHS–FeCo (3). The details are included in the Experimental Section.

Figure 2 shows representative transmission electron microscopy (TEM) images of (a) porous carbon cage (CHS) and (b) CHS–FeCo(2). One can see that hollow carbon cages were successfully produced by pyrolysis of the SiO_2@MF precursors followed by HF etching, with the wall thickness mostly in the range of 1.0 to 2.5 nm (Figure 2a inset) and the interior diameter consistent with that of the SiO_2 sphere templates (140 $\pm$ 27 nm, Figure S1). In high-resolution TEM measurements (Figure 2b inset), the CHS–FeCo samples showed no well-defined lattice fringes, suggesting the formation of only an amorphous carbon structure, as observed previously.[20f] Remarkably, the fact that no particulate objects were observed also suggests that the metal species were most likely atomically dispersed within the carbon matrix. This is consistent with elemental mapping results based on energy-dispersive X-ray analysis, where both Fe and Co were scattered within the carbon matrix, without apparent agglomeration (Figure 2d-h). In addition, one can see that nitrogen is also rather evenly dispersed within the carbon skeleton, suggesting successful doping of nitrogen in the carbon.

The porosity of the samples was then investigated by the nitrogen adsorption and desorption isotherm measurements (Figure S2a). The CHS–FeCo(2) sample can be seen to exhibit an apparent type IV hysteresis loop above 0.49 P/P_o, which is indicative of the formation of mesopores. In fact, the pores are mostly within the range of 1.0 to 2.5 nm, as depicted in the pore size distribution (Figure S2b). Furthermore, the specific

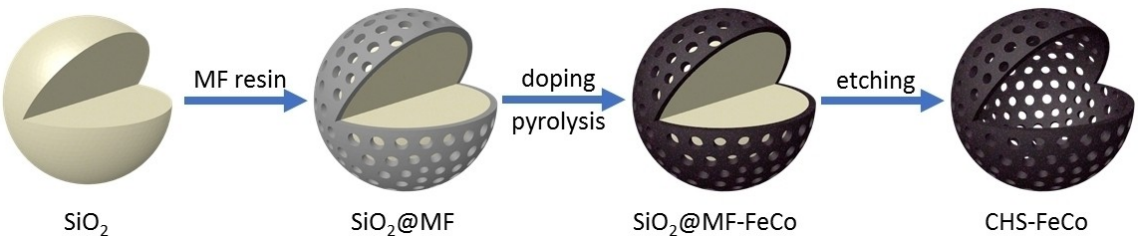

Figure 1. Schematic illustration of the preparation of CHS–FeCo.

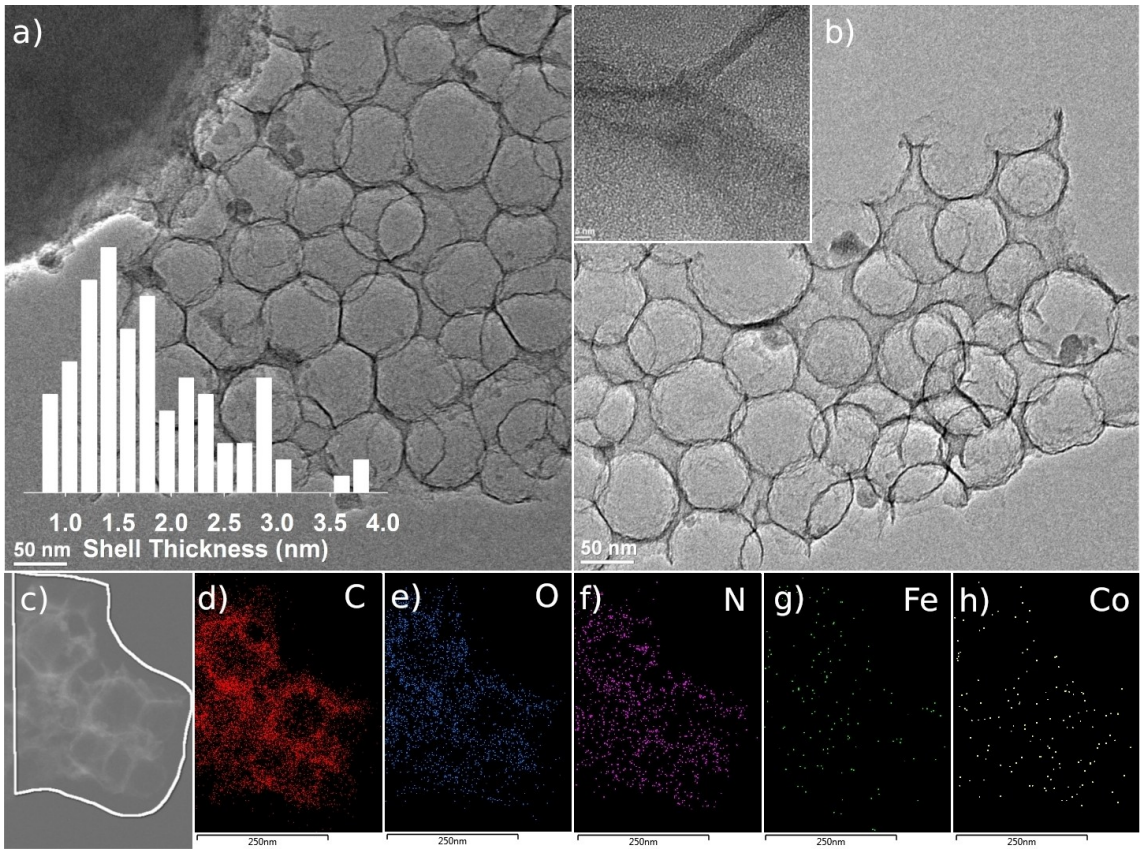

Figure 2. (a) Representative TEM image of CHS. Inset is the histogram of the shell thicknesses. (b) TEM image of CHS–FeCo(2). Inset is a high-resolution image of the sample (scale bar 5 nm). (c-h) Elemental maps of CHS–FeCo(2).

surface area based on the Brunauer-Emmett-Teller (BET) theory was estimated to be ca. 60 m^2/g.

XPS measurements were then conducted to probe the elemental composition of the carbon cages and the valence states of the elements. The survey spectra (Figure S3) show that the cages are mainly composed of carbon, nitrogen, and oxygen, as well as iron and cobalt in the case of the CHS–FeCo samples, with the exception of those doped with Fe or Co alone, which are also consistent with the elemental maps shown above in Figure 2d–h. In addition, based on the integrated peak areas, the elemental contents in the samples were quantitatively assessed. From Table S1, one can see that for the metal-free CHS sample, carbon accounts for about 72.74 at% of the total content, nitrogen 9.21 at% and oxygen 14.23 at%. With the addition of a single metal precursor, these elemental fractions remained almost unchanged, with a trace amount of metal species, 0.16 at% for Fe in CHS–Fe and 0.06 at% for Co in CHS–Co. For the bimetallic CHS–FeCo(1,2,3) series, whereas the N content was almost invariant at ca. 6%, the total metal content increased from 0.32 at% for CHS–FeCo (1) to 0.38 at% for CHS–FeCo(2) and to 0.49 at% for CHS–FeCo (3), with the Fe content at 0.27 at% for both CHS–FeCo(1) and CHS–FeCo(2) and 0.38 at% for CHS–FeCo(3), and the Co content at 0.05 at% for CHS–FeCo(1) and 0.11 at% for both CHS–FeCo(2) and CHS–FeCo(3).

High-resolution XPS scans for the C 1s, N 1s, Fe 2p, and Co 2p electrons are depicted in Figure 3. All C 1s scans (Figure 3a) exhibit a very similar shape and composition. Deconvolution yields a sharp peak at 284.5 eV, which can be assigned to graphitic (sp^2) carbon and provides evidence for successful carbonization of the melamine-formaldehyde resin, another one at 285.1 eV for sp^3-hybridized carbon (including N-bonded C), and two additional ones at 287.0 and 289.8 eV due to various forms of oxidized carbon that can be assigned to C=O, COOH, and π - π^* transitions.[22] Figure 3b shows the N 1s scans of the CHS, CHS–Fe, CHS–Co and CHS–FeCo(1,2,3) samples. For the latter, six distinct peaks at ca. 398.2, 398.9, 399.8, 400.8, and 401.7 eV (averaged from the series of samples, Table S2) can be resolved and assigned to pyridinic N, metal-N, pyrrolic, graphitic, and oxidized N, respectively (the small broad peak at 404.0 eV likely stems from chemisorbed NO_x species).[23] One can see that the integrated area (concentration) of the N-metal peak decreases with decreasing metal content in the samples and is completely absent in the metal-free CHS sample (Table S1 and S2).

The respective high-resolution scans of the Fe 2p and Co 2p electrons are depicted in Figure 3c and 3d, respectively. Since both metals contain, in their high spin forms, unpaired electrons in non-spherically symmetric orbitals, the scans do not only exhibit spin-orbit coupling, producing a larger $p_{3/2}$ and

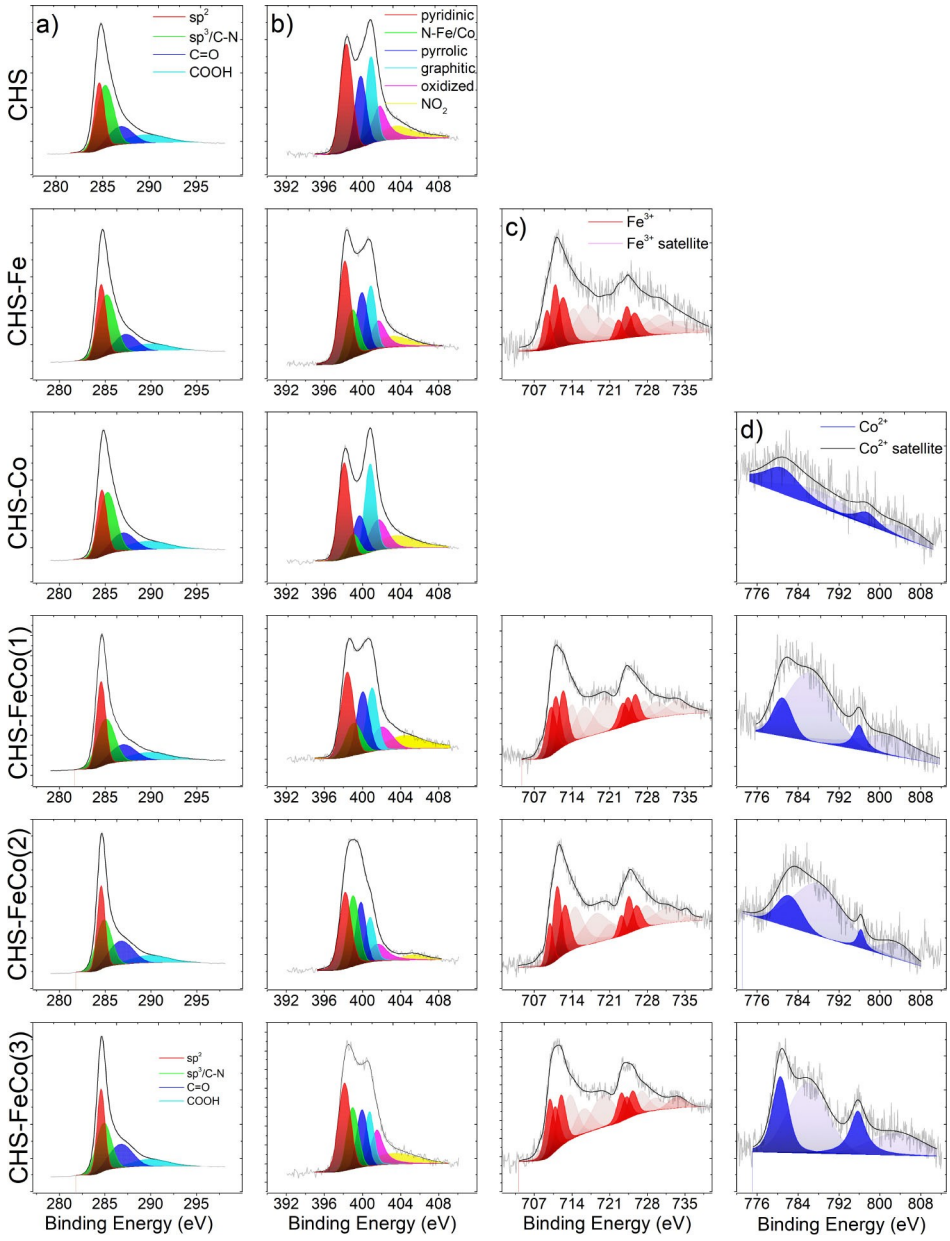

Figure 3. High-resolution XPS scans of the (a) C 1s, (b) N 1s, (c) Fe 2p, and (d) Co 2p electrons of CHS, CHS–Fe, CHS–Co, and CHS–FeCo(1,2,3) samples. Grey curves are experimental data, and colored peaks are deconvolution fits.

a smaller $p_{1/2}$ peak, but also spin multiplet splitting and various satellite features.[24] This is particularly prominent in the Fe 2p scans, whereas the intensity of the Co 2p peaks is too low to resolve individual spin multiplet peaks. The best fits for the Fe2p scans are based on Fe^{2+} multiplet patterns.[25] Similarly, the experimental data for Co is best fitted using a single set of Co^{2+} peaks and corresponding satellites,[26] noting that the peaks for Co^{2+} and Co^{3+} overlap to such an extent that it becomes impossible to resolve them reliably due to their low abundance.[24] Notably, the Fe $2p_{3/2}$ binding energy (Table S3) remains unchanged around 709.9 eV for all CHS–FeCo(1,2,3) samples, but somewhat higher than that (708.6 eV) for CHS–Fe. This binding energy is in the intermediate between those reported for Fe^{2+} and Fe^{3+},[24–25] indicating that the Fe species in the CHS–FeCo samples were likely Fe^{2+} in an electron-withdrawing environment, as compared to CHS–Fe, given that the precursor used was of the +2 oxidation state in all samples. Notably, the Co $2p_{3/2}$ binding energy can be estimated to be 779.8 eV for the samples; yet the low abundance of Co in combination with the overlap between the features of the different oxidation states makes it impossible to determine them precisely.[27] Lastly, high-resolution O 1s scans (Figure S4) suggest that no metal oxides are formed in the samples, as indicated by the absence of a corresponding peak between 529 and 530 eV (that is, the metal centers are embedded within the carbon matrix most likely forming M–N bonds).[28]

X-ray absorption near-edge structure (XANES) and extended X-ray absorption fine structure (EXAFS) analysis was then conducted to probe the electronic property and coordination environments of the metal centers. The Fe XANES curve in Figure 4a shows a fingerprint peak in the pre-edge region for the Fe foil at 7113 eV, which diminished markedly for the CHS–Fe and CHS–FeCo samples, implying that the Fe centers are non-metallic in the latter.[29] Additionally, one can see that both CHS–FeCo(2) and CHS–Fe exhibited a markedly higher absorption edge energy than the Fe foil, again, indicating a higher oxidation state of the Fe centers in CHS–Fe and CHS–FeCo than Fe(0). Furthermore, the fact that the absorption edge energy was slightly higher for CHS–FeCo(2) than for CHS–Fe is in good agreement with results from XPS measurements (Figure 3) where the Fe centers in the former were found to be situated in an electron-withdrawing environment, as compared to that in the latter. The same observation can be made for the Co XANEs profiles (Figure 4b), where the oxidation state of Co in CHS–FeCo is apparently higher than Co(0) in the Co foil.

Figure 4c shows the corresponding Fe FT-EXAFS spectra. The Fe foil can be seen to display two prominent peaks around 2 and 4.5 Å, due to the first and second shells of Fe–Fe.[30] These spectral features were totally absent in CHS–Fe and CHS–FeCo, which instead show a major peak below 2 Å and a minor one between 2 and 3 Å. Because of the absence of metal oxides in the CHS–Fe and CHS–FeCo samples, CHS–Fe was best fitted with a single Fe–N shell (Figure S5),[29] where the Fe–N bond length was estimated to be 1.96 Å with the average coordination number (CN) of 3.2 (Table S4). For CHS–FeCo(2), the best fit consisted of two shells, Fe–N and Fe–Co.[29] The Fe–N bond length (1.98 Å) was found to be rather consistent with that of CHS–Fe but with a markedly higher CN of 3.8 (Table S4). This suggests that CHS–FeCo(2) contained a significant number of FeN_4 moieties, which are known to be very active for ORR, while other samples contained mostly unsaturated FeN_3 sites that are less active.[31] In addition, the CHS–FeCo(2) sample contained Fe–Co bond which was found to be 2.98 Å in length with a CN of 1.3 (Table S4), suggesting Fe–Co pairing in the sample. In summary, EXAFS results suggest that the combination of Fe and Co results in a direct interaction between the two metal centers, with excess Fe present in the sample forming FeN_x (Table S1).

The electrocatalytic performance of the samples was then evaluated by rotating ring-disk electrode (RRDE) voltammetric measurements. From the polarization curves in Figure 5a, it is evident that the CHS–Co sample exhibited a very poor activity, with an onset potential (E_{onset}) of +0.81 V and half-wave potential ($E_{1/2}$) of +0.65 V, similar to metal-free CHS (E_{onset} = +0.80 V and $E_{1/2}$ = +0.67 V). The performance was substantially improved with the CHS–Fe sample (E_{onset} = +0.92 V), as Fe–N moiety has been known to be active towards ORR.[32] An even better performance was observed with the CHS–FeCo samples (Table S5), which varied in the order of CHS–FeCo(1) (E_{onset} = +0.89 V and $E_{1/2}$ = +0.74 V) < CHS–FeCo(3) (E_{onset} = +0.90 V and $E_{1/2}$ = +0.78 V) < CHS–FeCo(2) < (E_{onset} = +0.93 V and $E_{1/2}$ = +0.79 V). Consistent behaviors can be seen in the respective electron transfer numbers and H_2O_2% yields (Figure 5b and S6).

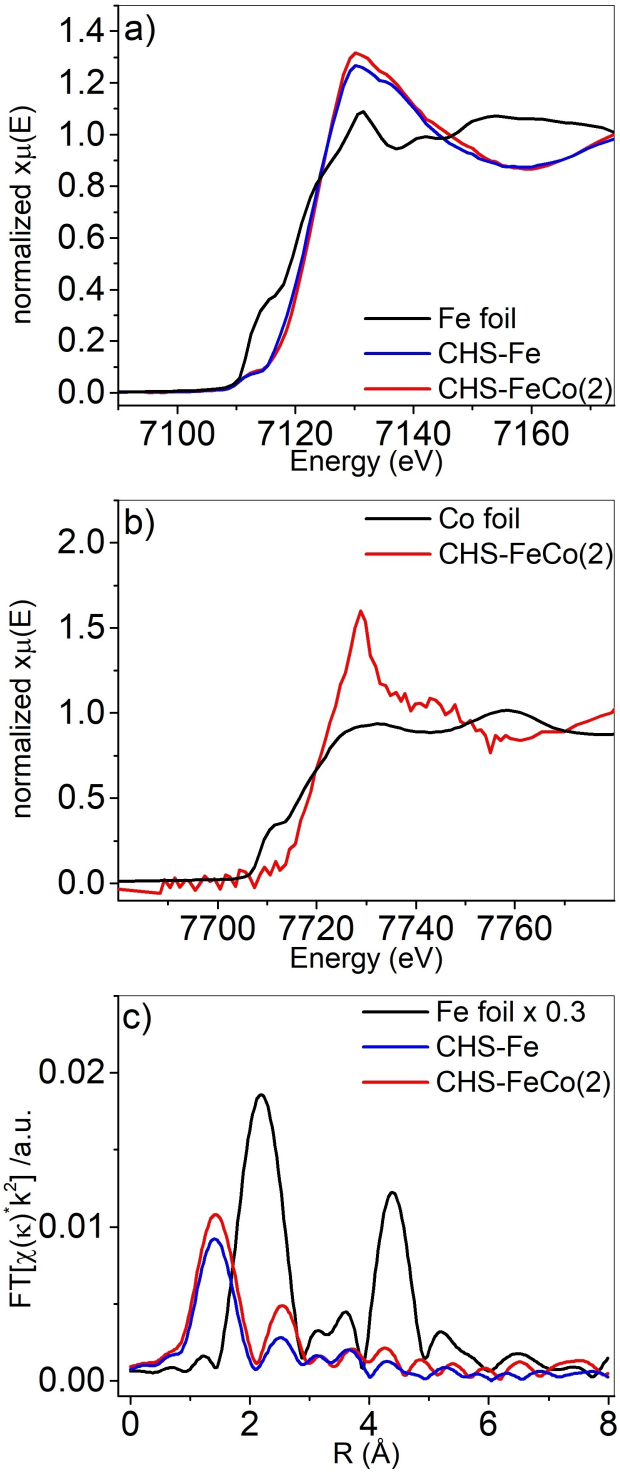

Figure 4. X-ray absorption spectroscopic studies. (a) Iron normalized X-ray absorption near edge structure data for CHS–Fe, CHS–FeCo(2), and Fe-foil. (b) Cobalt normalized X-ray absorption near edge structure data for CHS–FeCo(2) and Co-foil. (c) Fourier transform extended X-ray adsorption fine structure data for CHS–Fe, CHS–FeCo(2) and Fe-foil.

For instance, at +0.50 V, n = 3.61 and H_2O_2% = 19.5% for CHS–FeCo(1), 3.80 and 10% for CHS–FeCo(2) and CHS–FeCo(3). The corresponding Koutecký-Levich and Tafel plots are shown

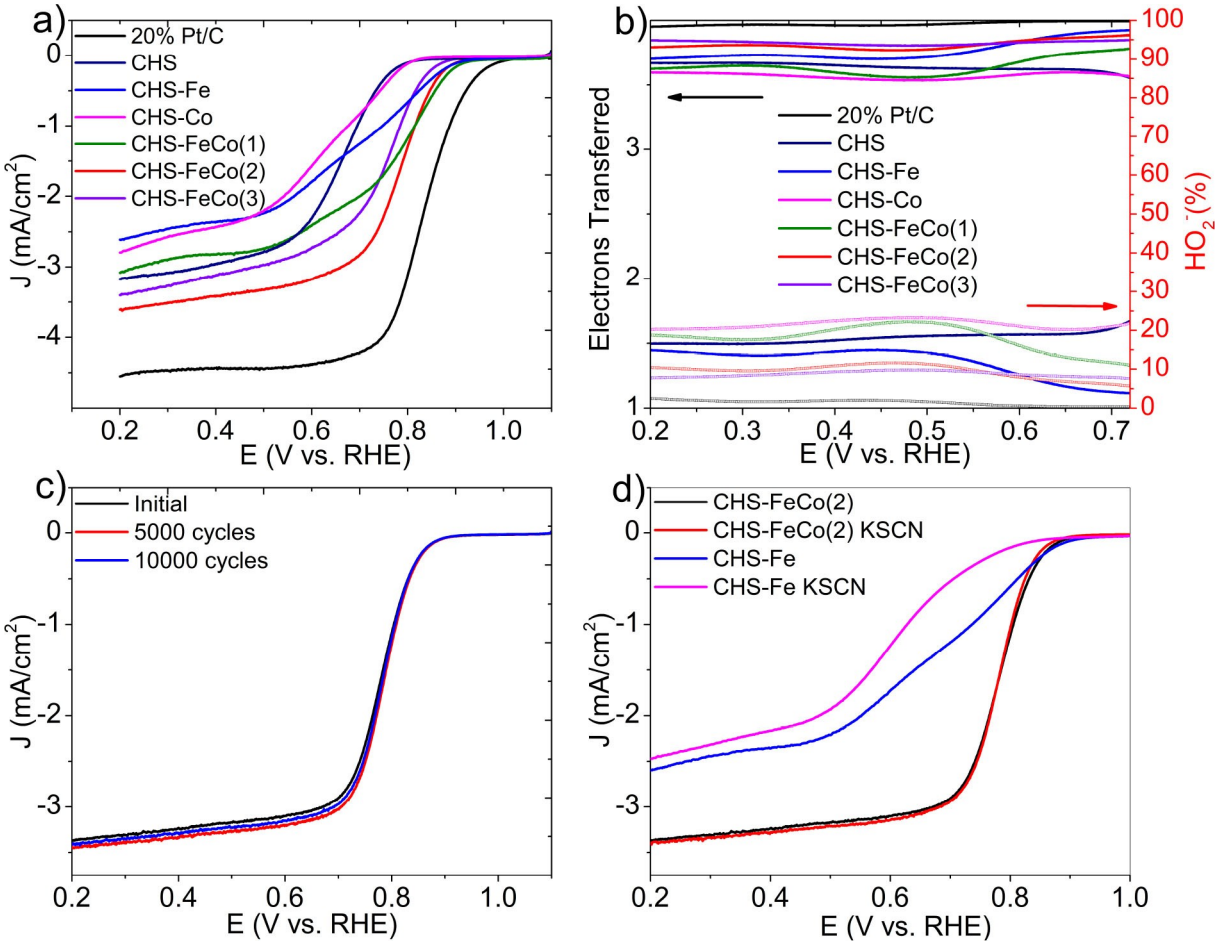

Figure 5. Polarization curves of various CHS samples at 1600 rpm and a potential scan rate of 10 mV/s in an oxygen-saturated 0.1 M KOH solution. (a) Comparison of CHS, CHS–Fe, CHS–Co, and CHS–FeCo(1,2,3). (b) Number of electron transfer (top, black arrow) and H_2O_2% yield (bottom, red arrow) for the various samples in (a). (c) Stability test of CHS–FeCo(2) for up to 10,000 potential cycles. (d) ORR polarization curves of CHS–FeCo(2) and CHS–Fe before and after the addition of KSCN to the electrolyte.

in Figure S6 and S7. All these results show that CHS–FeCo(2) stood out as the best catalyst among the series (with CHS–FeCo (3) being the close second), largely in line with the high contents of Fe–Co pairing in the samples (Table S1). This is most likely due to the synergistic effects of the two metal dopants, as evidenced in the above XPS and XAS measurements (Figure 3 and 4). Notably, such a promising performance is highly comparable or even superior to relevant carbon-based catalysts reported recently in the literature (Table S6), although it remains subpar as compared to that of Pt/C (Figure 5).

Interestingly, the ORR performance also varied with both the counterion and oxidation state of the metal salt precursors. From Figure S8, one can see that CHS–FeCo prepared with $FeSO_4$ as the precursor exhibited a markedly better ORR activity than those with $FeCl_2$, $FeCl_3$ and $Fe(acac)_3$. XPS analysis shows that the metal content of the samples was about eight times higher for the former (Figure S9), possibly due to the different thermal volatilities of the iron compounds.[33] However, the difference in metal content between the latter three was too small to account for their apparent difference of the catalytic performance. This suggests that the metal precursor used influences the chemical nature of the active sites, thereby enabling distinct catalytic pathways. Indications of such a chemical change have come from XPS and EXAFS analysis, suggesting that the direct interaction between the Fe and Co dopants in CHS–FeCo is absent in other samples. Further research is strongly desired to unravel the mechanistic correlation.

The stability of the catalysts was then tested by repeated potential sweeping. As shown in Figure 5c, the polarization curves remained virtually unchanged for up to 10,000 cycles. Such remarkable stability confirms the strong incorporation of the metal centers into the carbon skeletons. In addition to the stability test, the catalytic performance was examined when the electrolyte was poisoned with 10 mM KSCN (Figure 5d). It is well-known that the thiocyanate anion binds strongly and selectively to metals, both in nanoparticle and atomically dispersed forms, blocking access to the metal active centers and diminishing the electrocatalytic activity.[34] Interestingly, from Figure 5d one can see that CHS–FeCo(2) shows virtually no activity loss upon the addition of KSCN, whereas the activity of CHS–Fe deteriorated significantly, with the half-wave

potential shifted negatively by ca. 100 mV. The latter observation has been observed rather extensively in prior studies.[31] However, the resistance of CHS–FeCo(2) against thiocyanate poisoning has never been seen with any dual metal-based catalysts for ORR.

The structures of the CHS–FeCo(2) and CHS–Fe samples were then analyzed by XPS measurements before and after the KSCN poisoning tests (Figure 6). For CHS–Fe, the spectral results exhibit clear signs of KSCN poisoning, as demonstrated by the notable metal-sulfur (M–S) signature with an S 2p peak at the binding energy of 161.2 eV (Figure 6b).[35] Meanwhile, a new set of peaks emerged in the Fe 2p spectrum at 707.3, 707.7 and 708.5 eV, which can all be attributed to Fe(II) in Fe(II)-S bond (Figure 6a).[36] This poisoning led to a marked diminishment of the ORR activity of CHS–Fe. By contrast, no such S and Fe species can be found for CHS–FeCo(2) after KSCN treatment. One can see that the Fe(II) $2p_{1/2}$ binding energy exhibited only a slight variation from 709.90 to 709.19 eV, and the S 2p scan showed only a peak at 167.82 eV for SO_2 and another one at 164.4 eV for elemental S.[36] This suggests that SCN^- was mostly

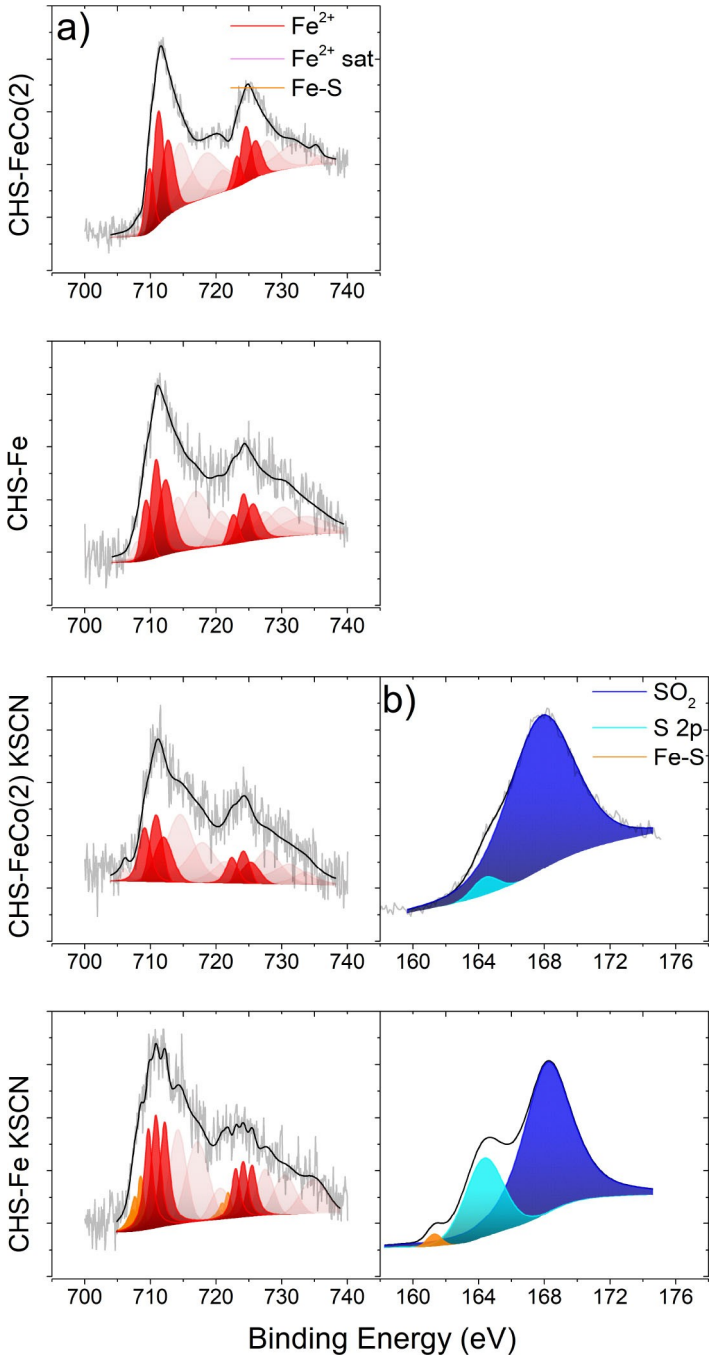

Figure 6. High-resolution XPS scans of the (a) Fe 2p and (b) S 2p electrons of CHS–FeCo(2) and CHS–Fe before and after the addition of KSCN. Grey curves are experimental data, and shaded peaks are deconvolution fits

likely oxidized by CHS–FeCo(2) to SO_2. The lack of KSCN poisoning of the CHS–FeCo(2) catalyst is in good agreement with the almost unchanged electrocatalytic activity (Figure 5d). Further studies are needed to unravel the mechanistic details.

3. Conclusion

In this study, dual metals (Fe and Co) and nitrogen-codoped carbon cages were prepared by controlled pyrolysis of a melamine-formaldehyde polymer shell supported on SiO_2 nanoparticle templates. TEM and X-ray absorption spectroscopic measurements suggested atomic dispersion of the metal centers within the carbon matrix and the synergistic interactions between the dual metal centers led to marked enhancement of the electrocatalytic activity towards ORR in alkaline media, as compared to the metal-free or monometal counterparts. Remarkably, the dual-metal sample exhibited apparent resistance against thiocyanate poisoning. Results from this study suggest that dual metal doping and the ensuing metal-metal interactions may be exploited as a unique strategy for further enhancement of ORR electrocatalysis by carbon-based nanocomposites.

Experimental Section

Chemicals

Tetraethyl orthosilicate (TEOS, 98%, Acros Organics), ammonium hydroxide (NH_4OH, 28%, Fisher Scientific), reagent alcohol (EtOH, absolute, Macron Fine Chemicals), melamine (99%, Acros Organics), formaldehyde (37% v/v, Acros Organics), sodium hydroxide (NaOH, Fisher Scientific), ferrous sulfate heptahydrate ($FeSO_4 \cdot 7H_2O$, Fisher Scientific), ferrous chloride tetrahydrate ($FeCl_2 \cdot 4H_2O$, Fisher Scientific), iron(III) acetylacetonate ($Fe(acac)_3$, Acros organics), ferric chloride hexahydrate ($FeCl_3 \cdot 6H_2O$, Fisher Scientific), cobalt(II) chloride hexahydrate ($CoCl_2 \cdot 6H_2O$, Fisher Scientific), hydrofluoric acid (HF, 48%, Fisher Scientific), and Pt/C (20 wt%, Alfa Aesar) were all used as received. Water was supplied from a Barnstead Nanopure Water System (18.3 MΩ cm).

Synthesis of silica nanoparticles

SiO_2 nanoparticles were synthesized by adopting a literature procedure.[37] Typically, 16 mL of NH_4OH and 0.6 mL of TEOS were added into 240 mL of EtOH to form a clear solution, which was magnetically stirred for 16 h at room temperature. The product (SiO_2 nanoparticles) was collected by centrifugation, vacuum dried, and stored for future use.

Synthesis of melamine-formaldehyde resin coated silica nanoparticles

A melamine-formaldehyde (MF) resin coating layer was grown onto the SiO_2 nanoparticles prepared above.[20f] In a typical synthesis, 0.189 g of melamine was dissolved in 30 mL of H_2O at 90 °C, into which were added 12.5 mg of SiO_2 nanoparticles, 795 μL of formaldehyde, and a catalytic amount of NaOH, and the mixture was stirred overnight. The product was collected by centrifugation and vacuum dried to yield melamine-formaldehyde resin coated silica nanoparticles (SiO_2@MF).

Synthesis of dual-metal and nitrogen-codoped hollow carbon spheres

The SiO_2@MF obtained above was then used to prepare dual metals and nitrogen-doped hollow carbon spheres.[23a] In brief, 50.0 mg of SiO_2@MF was soaked for several hours in an aqueous solution containing $FeSO_4$ and $CoCl_2$ at varied concentrations: (1) 1.8 mM for both $FeSO_4$ and $CoCl_2$, (2) 0.8 mM for $FeSO_4$ and 2.9 mM for $CoCl_2$, and (3) 0.4 mM for $FeSO_4$ and 3.2 mM for $CoCl_2$. The product was centrifuged, and vacuum dried before being placed in a tube furnace and heated to 800 °C for 1 h in a N_2 atmosphere at the heating rate of 10 °C/min (800 °C was identified as the optimal temperature, not shown). The obtained black powder was stirred in a 10% HF solution to remove the SiO_2 templates, yielding dual metals and nitrogen-codoped porous carbon cages. The three samples prepared at different Fe and Co loadings are denoted as CHS–FeCo(1), CHS–FeCo(2), and CHS–FeCo(3), respectively.

Six control samples were also prepared in the same manner. The first one (CHS) was derived directly by pyrolysis of SiO_2@MF without the soaking in any salt solution. The second sample (CHS–Fe) was prepared by soaking SiO_2@MF in a solution containing only $FeSO_4$ (3.6 mM); the third one (CHS–Co) was prepared by soaking SiO_2@MF in the solution contained only $CoCl_2$ (3.6 mM). The fourth sample (CHS–$FeCo_{FeCl2}$) was prepared by soaking SiO_2@MF in a solution containing $FeCl_2$ (0.8 mM) and $CoCl_2$ (2.9 mM). The fifth sample (CHS–$FeCo_{FeCl3}$) was prepared by soaking SiO_2@MF in a solution containing $FeCl_3$ (0.8 mM) and $CoCl_{2;}$ (2.9 mM) and the sixth sample (CHS–$FeCo_{Fe(acac)3}$) was prepared by soaking SiO_2@MF in a solution containing $Fe(acac)_3$ (0.8 mM) and $CoCl_2$ (2.9 mM).

Characterization

Transmission electron microscopy (TEM) images were acquired using a Philips CM300 microscope operated at 300 kV. Scanning electron microscopy (SEM) images were obtained on a FEI Quanta 3D field emission microscope operated at 10.0 kV. X-ray photoelectron spectroscopy (XPS) studies were conducted using a PHI5400/XPS instrument with an Al K_α source operated at 350 W and 10^{-9} Torr. XAS measurements were performed using the Sector 20-BM beamline of the Advanced Photon Source at Argonne National Laboratory (Argonne, IL). The beamline was equipped with a double-crystal Si(111) monochromator. A 12-element Ge fluorescence detector was used to collect spectra of the Fe and Co K edges. The energy was calibrated according to the absorption edge of a pure Fe or Co foil, as appropriate. Data processing and fitting were performed using WinXAS[38] and Analyzer v0.1 software, with scattering paths generated by FEFF8.[39] S_0^2 values for Fe (0.80) and Co (0.74) were obtained by fitting Fe and Co foil, respectively. Nitrogen adsorption-desorption isotherms were acquired at 77 K with a Micromeritics ASAP 2020 surface area and porosity analyzer.

Electrochemistry

All electrochemical tests were carried out on a CHI710 workstation in a three-electrode setup. A graphite rod was used as the counter electrode and a Ag/AgCl electrode in 1.0 M KCl was used as the reference electrode. This electrode was calibrated against a reversible hydrogen electrode (RHE), and all potentials in this study are reported in reference to this RHE. A rotating (gold) ring-(glassy carbon) disk electrode (RRDE, Pine Research Instruments) was used as the working electrode. In the collection experiment, the ring

potential was set at +1.5 V vs RHE. To prepare catalyst inks, 0.8 mg of the samples obtained above and 2.0 μL of 20% Nafion were added to 200 μL of a water-ethanol mixture (1:1 v/v). After sonication for at least 30 min, 5.0 μL of the ink was dropcast onto the glassy carbon disk, corresponding to a catalyst loading of 81.3 μg/cm^2. Once the catalyst film was dried, 3.0 μL of 20% Nafion was added to cover the catalyst layer, and the electrodes were immersed into electrolyte solutions for testing.

Acknowledgements

This work was supported in part by the National Science Foundation (CHE-1900235) and UC Merced MACES under the NASA MIRO program. TEM and XPS studies were carried out at the National Center for Electron Microscopy and Molecular Foundry, Lawrence Berkeley National Laboratory, which is supported by the US Department of Energy, as part of a user project. This research used resources of the Advanced Photon Source, operated for the U.S. Department of Energy (DOE) Office of Science by Argonne National Laboratory, and was supported by the U.S. DOE under Contract No. DE-AC02-06CH11357, and the Canadian Light Source and its funding partners.

Conflict of Interest

The authors declare no conflict of interest.

Keywords: silica nanoparticle · carbon cage · dual metal · nitrogen-doped · oxygen reduction reaction

[1] X. J. Zhou, J. L. Qiao, L. Yang, J. J. Zhang, *Adv. Energy Mater.* **2014**, *4,* 1301523.
[2] Z. Yang, H. Nie, X. Chen, S. Huang, *J. Power Sources* **2013**, *236*, 238–249.
[3] J. L. Fernández, V. Raghuveer, A. Manthiram, A. J. Bard, *J. Am. Chem. Soc.* **2005**, *127*, 13100–13101.
[4] a) K. Yamamoto, T. Imaoka, W.-J. Chun, O. Enoki, H. Katoh, M. Takenaga, A. Sonoi, *Nat. Chem.* **2009**, *1*, 397; b) Y.-J. Wang, N. Zhao, B. Fang, H. Li, X. T. Bi, H. Wang, *Chem. Rev.* **2015**, *115*, 3433–3467.
[5] a) K. Gong, F. Du, Z. Xia, M. Durstock, L. Dai, *Science* **2009**, *323*, 760–764; b) L. Jian, Q. S. Zhang, B. H. Sandy, L. G. Q. (Max), *Angew. Chem. Int. Ed.* **2010**, *122*, 5101–5105; c) K. Ai, Y. Liu, C. Ruan, L. Lu, G. Lu, *Adv. Mater.* **2013**, *25*, 998–1003.
[6] Y. Li, Y. Zhao, H. Cheng, Y. Hu, G. Shi, L. Dai, L. Qu, *J. Am. Chem. Soc.* **2011**, *134*, 15–18.
[7] J. Masa, W. Xia, M. Muhler, W. Schuhmann, *Angew. Chem. Int. Ed.* **2015**, *54*, 10102–10120; *Angew. Chem.* **2015**, *127*, 10240–10259.
[8] a) C. H. Choi, S. H. Park, S. I. Woo, *ACS Nano* **2012**, *6*, 7084–7091; b) X. Fang, X. Zhao, W. Fang, C. Chen, N. Zheng, *Nanoscale* **2013**, *5*, 2205–2218.
[9] a) Z. Shi, H. Liu, K. Lee, E. Dy, J. Chlistunoff, M. Blair, P. Zelenay, J. Zhang, Z.-S. Liu, *J. Phys. Chem. C* **2011**, *115*, 16672–16680; b) F. Jaouen, M. Lefèvre, J.-P. Dodelet, M. Cai, *J. Phys. Chem. B* **2006**, *110*, 5553–5558; c) K. Strickland, E. Miner, Q. Jia, U. Tylus, N. Ramaswamy, W. Liang, M.-T. Sougrati, F. Jaouen, S. Mukerjee, *Nat. Commun.* **2015**, *6*, 7343; d) H. T. Chung, J. H. Won, P. Zelenay, *Nat. Commun.* **2013**, *4*, 1922.
[10] a) K. P. Singh, E. J. Bae, J.-S. Yu, *J. Am. Chem. Soc.* **2015**, *137*, 3165–3168; b) J. H. Zagal, M. T. Koper, *Angew. Chem. Int. Ed.* **2016**, *55*, 14510–14521; *Angew. Chem.* **2016**, *128*, 14726–14738.
[11] a) H. Schulenburg, S. Stankov, V. Schünemann, J. Radnik, I. Dorbandt, S. Fiechter, P. Bogdanoff, H. Tributsch, *J. Phys. Chem. B* **2003**, *107*, 9034–9041; b) Q. Zhou, C. M. Li, J. Li, J. Lu, *J. Phys. Chem. C* **2008**, *112*, 18578–18583; c) S. Maldonado, K. J. Stevenson, *J. Phys. Chem. B* **2004**, *108*, 11375–11383; d) G. Wu, K. L. More, C. M. Johnston, P. Zelenay, *Science* **2011**, *332*, 443–447; e) E. Proietti, F. Jaouen, M. Lefèvre, N. Larouche, J. Tian, J. Herranz, J.-P. Dodelet, *Nat. Commun.* **2011**, *2*, 416; f) J. Chlistunoff, *J. Phys. Chem. C* **2011**, *115*, 6496–6507; g) G. Wu, K. Artyushkova, M. Ferrandon, A. J. Kropf, D. Myers, P. Zelenay, *ECS Trans.* **2009**, *25*, 1299–1311.
[12] a) A. Mehmood, J. Pampel, G. Ali, H. Y. Ha, F. Ruiz-Zepeda, T. P. Fellinger, *Adv. Energy Mater.* **2018**, *8*, 1701771; b) N. D. Leonard, S. Wagner, F. Luo, J. Steinberg, W. Ju, N. Weidler, H. Wang, U. I. Kramm, P. Strasser, *ACS Catal.* **2018**, *8*, 1640–1647; c) Y. Peng, B. Lu, S. Chen, *Adv. Mater.* **2018**, *30*, 1801995; d) Y. Qian, P. Du, P. Wu, C. Cai, D. F. Gervasio, *J. Phys. Chem. C* **2016**, *120*, 9884–9896.
[13] a) G.-T. Fu, C. Liu, Q. Zhang, Y. Chen, Y.-W. Tang, *Sci. Rep.* **2015**, *5*, 13703; b) L. Bu, N. Zhang, S. Guo, X. Zhang, J. Li, J. Yao, T. Wu, G. Lu, J.-Y. Ma, D. Su, *Science* **2016**, *354*, 1410–1414; c) Z. Zhu, Y. Zhai, S. Dong, *ACS Appl. Mater. Interfaces* **2014**, *6*, 16721–16726; d) Y. H. Han, Y. G. Wang, W. X. Chen, R. R. Xu, L. R. Zheng, J. Zhang, J. Luo, R. A. Shen, Y. Q. Zhu, W. C. Cheong, C. Chen, Q. Peng, D. S. Wang, Y. D. Li, *J. Am. Chem. Soc.* **2017**, *139*, 17269–17272; e) T. He, Y. Q. Zhang, Y. Chen, Z. Z. Zhang, H. Y. Wang, Y. F. Hu, M. Liu, C. W. Pao, J. L. Chen, L. Y. Chang, Z. F. Sun, J. Xiang, Y. Zhang, S. W. Chen, *J. Mater. Chem. A* **2019**, *7*, 20840–20846; f) T. He, B. Z. Lu, Y. Chen, Y. Wang, Y. Q. Zhang, D. L. Davenport, A. P. Chen, C.-W. Pao, M. Liu, Z. F. Sun, A. Stram, A. Mordaunt, J. Velasco Jr., P. Ping, Y. Zhang, S. W. Chen, *Research* **2019**, 6913585.
[14] H. Xue, J. Tang, H. Gong, H. Guo, X. Fan, T. Wang, J. He, Y. Yamauchi, *ACS Appl. Mater. Interfaces* **2016**, *8*, 20766–20771.
[15] a) B. Lu, L. Guo, F. Wu, Y. Peng, J. E. Lu, T. J. Smart, N. Wang, Y. Z. Finfrock, D. Morris, P. Zhang, *Nat. Commun.* **2019**, *10*, 631; b) A. Zitolo, V. Goellner, V. Armel, M.-T. Sougrati, T. Mineva, L. Stievano, E. Fonda, F. Jaouen, *Nat. Mater.* **2015**, *14*, 937; c) J.-D. Yi, R. Xu, Q. Wu, T. Zhang, K.-T. Zang, J. Luo, Y.-L. Liang, Y.-B. Huang, R. Cao, *ACS Energy Lett.* **2018**, *3*, 883–889.
[16] L. Lin, Z. K. Yang, Y.-F. Jiang, A.-W. Xu, *ACS Catal.* **2016**, *6*, 4449–4454.
[17] a) J.-Y. Choi, R. S. Hsu, Z. Chen, *J. Phys. Chem. C* **2010**, *114*, 8048–8053; b) Q. Lin, X. Bu, A. Kong, C. Mao, F. Bu, P. Feng, *Adv. Mater.* **2015**, *27*, 3431–3436.
[18] J. Y. Cheon, T. Kim, Y. Choi, H. Y. Jeong, M. G. Kim, Y. J. Sa, J. Kim, Z. Lee, T.-H. Yang, K. Kwon, *Sci. Rep.* **2013**, *3*, 2715.
[19] C. Liang, Z. Li, S. Dai, *Angew. Chem. Int. Ed.* **2008**, *47*, 3696–3717; *Angew. Chem.* **2008**, *120*, 3754–3776.
[20] a) W. Yang, T.-P. Fellinger, M. Antonietti, *J. Am. Chem. Soc.* **2010**, *133*, 206–209; b) W. Niu, L. Li, X. Liu, N. Wang, J. Liu, W. Zhou, Z. Tang, S. Chen, *J. Am. Chem. Soc.* **2015**, *137*, 5555–5562; c) W. Niu, L. Li, J. Liu, N. Wang, W. Li, Z. Tang, W. Zhou, S. Chen, *Small* **2016**, *12*, 1900–1908; d) W. Niu, L. Li, N. Wang, S. Zeng, J. Liu, D. Zhao, S. Chen, *J. Mater. Chem. A* **2016**, *4*, 10820–10827; e) W. Niu, L. Li, S. Chen, *J Electrochem* **2017**, *23*, 110–122; f) B. Lu, T. J. Smart, D. Qin, J. E. Lu, N. Wang, L. Chen, Y. Peng, Y. Ping, S. Chen, *Chem. Mater.* **2017**, *29*, 5617–5628.
[21] S. Mou, Y. Lu, Y. Jiang, *Appl. Surf. Sci.* **2016**, *384,* 258–262.
[22] a) Z. Yang, M. Xu, Y. Liu, F. He, F. Gao, Y. Su, H. Wei, Y. Zhang, *Nanoscale* **2014**, *6*, 1890–1895; b) S. Kundu, Y. Wang, W. Xia, M. Muhler, *J. Phys. Chem. C* **2008**, *112*, 16869–16878.
[23] a) R. Zhang, S. He, Y. Lu, W. Chen, *J. Mater. Chem. A* **2015**, *3*, 3559–3567; b) A. Sarapuu, L. Samolberg, K. Kreek, M. Koel, L. Matisen, K. Tammeveski, *J. Electroanal. Chem.* **2015**, *746*, 9–17; c) H. Zhong, H. Zhang, S. Liu, C. Deng, M. Wang, *ChemSusChem* **2013**, *6*, 807–812.
[24] M. C. Biesinger, B. P. Payne, A. P. Grosvenor, L. W. Lau, A. R. Gerson, R. S. C. Smart, *Appl. Surf. Sci.* **2011**, *257*, 2717–2730.
[25] A. Grosvenor, B. Kobe, M. Biesinger, N. McIntyre, *Surf. Interface Anal.* **2004**, *36*, 1564–1574.
[26] Y. Chen, S. Zhao, Z. Liu, *Phys. Chem. Chem. Phys.* **2015**, *17*, 14012–14020.
[27] C. Powell, *Appl. Surf. Sci.* **1995**, *89*, 141–149.
[28] J.-C. Dupin, D. Gonbeau, P. Vinatier, A. Levasseur, *Phys. Chem. Chem. Phys.* **2000**, *2*, 1319–1324.
[29] Y. Chen, S. Ji, Y. Wang, J. Dong, W. Chen, Z. Li, R. Shen, L. Zheng, Z. Zhuang, D. Wang, *Angew. Chem. Int. Ed.* **2017**, *56*, 6937–6941; *Angew. Chem.* **2017**, *129*, 7041–7045.
[30] L. Cao, W. Liu, Q. Luo, R. Yin, B. Wang, J. Weissenrieder, M. Soldemo, H. Yan, Y. Lin, Z. Sun, *Nature* **2019**, *565*, 631.
[31] Z. Huang, H. Pan, W. Yang, H. Zhou, N. Gao, C. Fu, S. Li, H. Li, Y. Kuang, *ACS Nano* **2018**, *12*, 208–216.
[32] a) L. T. Song, Z. Y. Wu, F. Zhou, H. W. Liang, Z. Y. Yu, S. H. Yu, *Small* **2016**, *12*, 6398–6406; b) Y. Wang, A. Kong, X. Chen, Q. Lin, P. Feng, *ACS Catal.* **2015**, *5*, 3887–3893.

[33] J. V. Hoene, R. G. Charles, W. M. Hickam, *J. Phys. Chem.* **1958**, *62*, 1098–1101.
[34] a) Q. Wang, Z.-Y. Zhou, Y.-J. Lai, Y. You, J.-G. Liu, X.-L. Wu, E. Terefe, C. Chen, L. Song, M. Rauf, *J. Am. Chem. Soc.* **2014**, *136*, 10882–10885; b) M. S. Thorum, J. M. Hankett, A. A. Gewirth, *J. Phys. Chem. Lett.* **2011**, *2*, 295–298; c) J. A. Varnell, C. Edmund, C. E. Schulz, T. T. Fister, R. T. Haasch, J. Timoshenko, A. I. Frenkel, A. A. Gewirth, *Nat. Commun.* **2016**, *7*, 12582.
[35] S. Niu, W. J. Jiang, T. Tang, L. P. Yuan, H. Luo, J. S. Hu, *Adv. Funct. Mater.* **2019**, *29*, 1902180.
[36] W. Han, M. Gao, *Cryst. Growth Des.* **2008**, *8*, 1023–1030.
[37] T. Harada, S. Ikeda, Y. H. Ng, T. Sakata, H. Mori, T. Torimoto, M. Matsumura, *Adv. Funct. Mater.* **2008**, *18*, 2190–2196.
[38] T. Ressler, *J. Synchrotron Radiat.* **1998**, *5*, 118–122.
[39] A. Ankudinov, B. Ravel, J. Rehr, S. Conradson, *Phys. Rev. B* **1998**, *58*, 7565.

Manuscript received: December 15, 2019
Revised manuscript received: April 8, 2020
Accepted manuscript online: April 9, 2020
Version of record online: May 5, 2020